J. Phys. B: At. Mol. Opt. Phys. **43** (2010) 155002 (10pp) doi:10.1088/0953-4075/43/15/155002

Box traps on an atom chip for one-dimensional quantum gases

J J P van Es[1], P Wicke[1], A H van Amerongen[1], C Rétif[2], S Whitlock[1] and N J van Druten[1]

[1] Van der Waals-Zeeman Institute, University of Amsterdam, Valckenierstraat 65-67, 1018 XE Amsterdam, The Netherlands
[2] FOM Institute for Atomic and Molecular Physics (AMOLF), Science Park 104, 1098 XG Amsterdam, The Netherlands

E-mail: N.J.vanDruten@uva.nl

Received 24 February 2010, in final form 31 May 2010
Published 7 July 2010
Online at stacks.iop.org/JPhysB/43/155002

Abstract
We present the implementation of tailored trapping potentials for ultracold gases on an atom chip. We realize highly elongated traps with box-like confinement along the long, axial direction combined with conventional harmonic confinement along the two radial directions. The design, fabrication and characterization of the atom chip and the box traps are described. We load ultracold ($\lesssim$1 μK) clouds of ^{87}Rb in a box trap, and demonstrate Bose-gas focusing as a means to characterize these atomic clouds in arbitrarily shaped potentials. Our results show that box-like axial potentials on atom chips are very promising for studies of one-dimensional quantum gases.

(Some figures in this article are in colour only in the electronic version)

1. Introduction

Microelectromagnetic traps produced using atom chips allow for extremely tight confinement and precise control of ultracold atoms and quantum degenerate gases [1–3]. These chips typically consist of lithographically defined wire patterns on a substrate which carry modest currents to create stable and tailor-made magnetic potentials for controlling atomic motion on the micrometre scale. The success of atom chips is due to the close proximity of the atoms to the field-producing elements which allow for high field gradients and tight confinement. For this reason, atom chips are also versatile tools for fundamental studies of quantum gases in one dimension [4–10].

The one-dimensional Bose gas exhibits remarkable phenomena that are not present in either 2D or 3D [11, 12]. Further interest stems from the availability of exact solutions for the many-body eigenstates and corresponding thermodynamics [13–18]. Almost all experimental work in this direction has employed high-aspect-ratio harmonic potentials. The strong *radial* harmonic confinement allows one to treat the gas as being effectively one-dimensional [19] along the axial direction, as long as the relevant energy scales are below the radial excitation energy, $\hbar\omega_\perp$. However, the *axial* harmonic confinement can be disadvantageous, since it leads to a spatially inhomogeneous density distribution, for which a comparison to the above exact theoretical treatments necessarily relies on the local-density approximation. In contrast, exact solutions do exist for the limiting case of a true box potential with infinitely steep walls [20, 21]. The ideal Bose gas also behaves rather differently in a box when compared to a harmonic trap [22–24]. Furthermore, some interesting features of interacting 1D gases, such as the quantum decoherent regime [17, 25], are limited to a relatively narrow range of temperatures and densities. In an axially harmonic trap, this will typically limit the fraction of the cloud that is in the regime of interest. A box-like *optical* trap in one dimension was recently realized for Bose–Einstein condensates (BECs) [26]. Atom chips hold the promise of simpler and more robust access to tailored axial potentials by employing specifically designed wire patterns [4, 5].

In this paper we demonstrate the experimental implementation of simple box-shaped axial potentials for studying one-dimensional gases on an atom chip. We describe in some detail the design, fabrication and characterization of our atom chips. These chips have already been successfully

used in experiments on one-dimensional Bose gases [9], and on the character of radio-frequency-dressed potentials [27]. We extend the technique of Bose-gas focusing [9, 28, 29] to box-like axial traps, and show that it provides an accurate measure of the energy distribution of atoms in these traps.

The outline of this paper is as follows. In section 2 we discuss the basic trapping geometry used to produce the box-shaped axial potentials. Typical experimental conditions allow access to the one-dimensional regime. In section 3 we describe in detail the fabrication process used to realize our atom chips. This section also includes a description of the various trapping geometries on the chip, including several box traps. In section 4, we describe experiments with ultracold atoms loaded into one of the box-shaped traps. This allows for the resulting magnetic potentials to be characterized. We analyse the technique of Bose-gas focusing from box-shaped trapping potentials and demonstrate its experimental use. We discuss some implications of our results and conclude in section 5.

2. Trapping geometry

One of the simplest trapping geometries for atoms consists of the field of a straight current-carrying wire combined with a uniform bias field oriented perpendicular to the wire direction [1–3]. The fields cancel at a position determined by the bias field, producing a quadrupolar field in the plane orthogonal to the wire, and a minimum field line parallel to the wire which can be used to guide atoms. The high field gradients possible in close proximity to the wire (which scale as r^{-2}) allow for tight confinement in the transverse directions. In order to produce a trap, full three-dimensional confinement is required. This is typically achieved by bending the wire into a *Z*-shape, with a long central segment and two segments at right angles, the latter being referred to as end wires. The end wires add a spatially varying field component oriented along the central segment of the wire which provides longitudinal confinement to the atoms. Typically the longitudinal potential is weak compared to the transverse confinement resulting in a highly elongated trap with a trap frequency ratio ($\omega_\perp/\omega_\parallel$) of a few hundred.

The *Z*-wire geometry has been extremely powerful for preparing ultracold atoms and BECs on atom chips in various experiments [1–3]. An important application is in generating high-aspect-ratio traps to investigate quantum gases in the 1D regime [6–10]. The drawback of the *Z*-wire for this application, however, is the inherent harmonic confinement in the longitudinal direction which limits the possible length of the studied systems and results in a spatially inhomogeneous atomic density requiring approximate theoretical treatments. Alternative wire geometries have been proposed to create long box-shaped axial potentials with nearly constant potential energy at the trap minimum, combined with tight harmonic confinement in the transverse directions [4, 5]. The wire patterns we have produced to create box-trap geometries of various dimensions are shown in figure 1. The basic trap is created by a long, straight and thin wire combined with a perpendicular bias field for transverse confinement, and two 'wiggles' positioned at both ends of the wire. Each wiggle

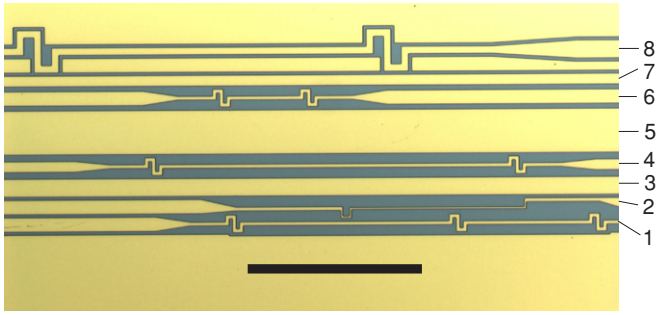

Figure 1. Optical microscope image of the central section of an atom chip. The chip hosts a series of microwires of various geometries for creating one-dimensional traps and box-shaped potentials. The length of the scale bar is 500 μm. The numbers at the right identify the atom chip wires and correspond to the numbers in table 1.

consists of two opposing notches in the trapping wire which generate end caps for the trapping potential, eliminating the need for end wires.

We first describe the field produced by such a box wire geometry. Current through a single wiggle produces a rapidly decaying magnetic field component oriented along the wire which produces a good approximation of a hard-wall potential for the atoms. The result can be accurately modelled by the field of two anti-aligned magnetic dipoles separated by a distance $\sqrt{2}b$ and with an effective magnetic moment Ib^2 each, where I is the wire current and b is the characteristic dimension (extension) of the wiggle. For small b the two dipoles combine to produce a field with quadrupole character:

$$\vec{B}_w = \begin{pmatrix} B_x \\ B_y \\ B_z \end{pmatrix} \approx \frac{3\mu_0 I b^3}{4\pi r^7} \begin{pmatrix} z(4x^2 - 5xy - y^2 - z^2) \\ z(x^2 + 5xy - 4y^2 + z^2) \\ (y - x)(x^2 + y^2 - 4z^2) \end{pmatrix}, \quad (1)$$

where $\mu_0 = 4\pi \times 10^{-7}$ H m^{-1} is the magnetic permeability of vacuum, $r = \sqrt{x^2 + y^2 + z^2}$ is the distance from the wiggle, x is the distance from the wiggle in the direction of the wire, y is the distance along the chip surface orthogonal to the wire and z is the distance from the chip surface. The potential experienced by the atoms trapped above the wire ($y = 0$) is determined predominately by the B_x field component which decays as $b^3 z/x^5$, where b and z are typically 20 μm. This is rapid compared to the end wire of a *Z*-trap (which decays relatively slowly, as z/x^2); therefore, the wiggle results in a harder potential wall. In a trap the transverse field components B_y, B_z produced by the wiggle are much smaller than the applied bias field and simply cause small displacements of the quadrupolar field in the y, z plane; these can be neglected in most applications.

The box-shaped potential is created by positioning two wiggles in a long straight wire. In this case the trapping field can be written as

$$\vec{B}_{\text{box}} = \vec{B}_w(x - L/2, y, z) + \vec{B}_w(x + L/2, y, z) + \vec{B}_l(x, y, z) + \vec{B}_b \quad (2)$$

where L is the length of the central segment between the wiggles, $\vec{B}_l$ is the field of the long wire (excluding the wiggles) and $\vec{B}_b$ is the bias field. Near $x = 0$, the longitudinal

potential consists of a vanishingly small curvature which scales as $b^3 z/L^7$. This should be compared with the longitudinal potential of a Z-trap with a central segment of length L which results in a harmonic potential with a larger axial curvature $\propto z/L^4$. The full form of the magnetic field (equations (1) and (2)) is relevant for experiments involving rf-dressed potentials, where the coupling of the rf field depends on the local orientation of the static field.

Such box traps hold great promise for studying quantum gases in the one-dimensional regime. To illustrate this we discuss the numbers involved in a typical experiment. Using ^{87}Rb atoms in the state $(F, m_F) = (2, 2)$ (scattering length $a = 5.24$ nm), trapped 20 μm above a 10 μm wide wire carrying 0.5 A of current, the radial trapping frequency would be $\omega_\perp = 2\pi \times 30$ kHz, and the radial size of the ground state $l_\perp = (\hbar/m\omega_\perp)^{1/2}$ would be 62 nm. The Lieb–Liniger parameter can be expressed as $\gamma = 2a/\ell_\perp^2 n_1$, with n_1 the linear density [19]. This parameter describes the crossover from the weakly interacting regime $\gamma < 1$ to the strongly interacting regime $\gamma > 1$ and would have a value of 1 at a linear density $n_1 = 2.7\ \mu\text{m}^{-1}$. The maximum length of a cloud in the 1D regime (temperature T, and chemical potential μ smaller than $\hbar\omega_\perp$) can now be estimated by calculating the length over which the axial trapping potential increases at most $\hbar\omega_\perp$ with respect to its minimum. For wiggles with $b = 20\,\mu$m separated by 1 mm, as in wire 4 in figure 1, this leads to a length of 0.73 mm ($\approx$1800 atoms at $\gamma = 1$). Further increasing the distance between the wiggles would allow a proportional increase in the length of the cloud and in the total number of atoms trapped. In comparison, for a Z-shaped wire with a central segment of 1 mm length, the higher harmonic axial confinement leads to an axial trapping frequency of 17.6 Hz, and a resulting cloud length of 100 μm, limiting the number of atoms to below 180 for a cloud with $n_1 = 2.7\ \mu\text{m}^{-1}$ at its centre.

3. Chip fabrication

This section describes the fabrication of our chip, focusing on the production of long, straight and high-quality micrometre-sized wires for producing magnetic potentials. The chips were produced and characterized using the facilities of the Amsterdam nanoCenter. We describe in some detail the fabrication recipe, the wire pattern design, characterization of the produced chips and the assembly used to support the chip. Further details can be found in [30, 31].

Two key factors played an important role in choosing the fabrication process. Firstly, we require well-defined and smooth magnetic potentials which can be accurately calculated from the corresponding conductor geometry to determine relevant trap parameters. The techniques chosen for the fabrication to a large extent determine the quality of the current-carrying wires and subsequently the smoothness of the resulting magnetic potentials [1–3, 32, 33]. It is also important that the wires are relatively thin and the atoms can be trapped close to the surface where large field gradients provide maximum radial confinement. Second, we desire a simple fabrication process in order to save time mastering the procedure and to allow many chip designs to be implemented in a short time. For this reason we designed a simple single-layer chip with only a limited number of wire patterns tailored for experiments with quantum gases in the one-dimensional regime and with box potentials. The equipment used to produce these chips is commonly available in any cleanroom facility.

We chose a 1.8 μm thick evaporated gold layer for the conductors and a 300 μm thick silicon substrate. Evaporated gold films on silicon substrates patterned using photolithographic lift-off techniques are known to produce high-quality wires with smoother surfaces as compared with electroplated wires [32–36]. Additionally, these materials have good thermal conductivity and the advantage that ample experience processing them is often available. At the centre of the chip we placed a 125 μm broad Z-wire with length $L = 3$mm (figure 1, wire 5), which is used to produce a deep magnetic trap for initial trapping and evaporative cooling of atoms to the BEC regime. This wire has a resistance of 0.72 Ω and is capable of carrying $\sim$2.5 A continuous current (maximum current density $\geqslant 10^6$ A cm^{-2}). The associated power dissipation of 4.5 W is sufficiently low so that conduction through the silicon substrate keeps the temperature below 80 °C. As the evaporated gold layer is relatively thick by microfabrication standards, we use two layers of resist. The top layer is a photo-sensitive resist patterned using optical lithography. The bottom layer is a lift-off resist used to create the insulating channels and as a spacer to prevent the top layer from being buried under the gold. During development the lower resist layer dissolves faster than the top layer, naturally generating an undercut (figure 2(a)). A layer of gold is then deposited using metal vapour deposition. By virtue of the overhang the edges of the deposited gold are well defined, while the open structure allows exposure to a solvent. The solvent dissolves the resist, effectively removing the gold lying on top of it, leaving only the patterned gold layer on the silicon substrate. Electrical insulation between the chip wires is through the resistivity of the silicon and the native silicon-oxide layer produced by exposure to air. We choose to keep the chip surface area large (25×16 mm^2 limited by the CF40 vacuum flange) and gold coated to allow for the reflection of laser beams. The reflective surface is used for a mirror magneto-optical trap (MOT) to collect atoms from background vapour. The small insulating channels between the wires produce negligible scattering of the reflected light and do not affect normal MOT operation.

3.1. Microfabrication recipe

(1) *Substrate preparation.* Substrates are cut from 3 inch silicon wafers with a (1-1-1) crystal orientation, a thickness of 300 μm and a resistivity of >4000 Ω cm. Atom chip substrates were produced from the wafers by laser cutting to dimensions of 24.63×16.00 mm^2. We clean the substrate prior to microfabrication in a heated mixture of ammonia and hydrogen peroxide solution to remove possible Si debris and organic contamination from the surface.

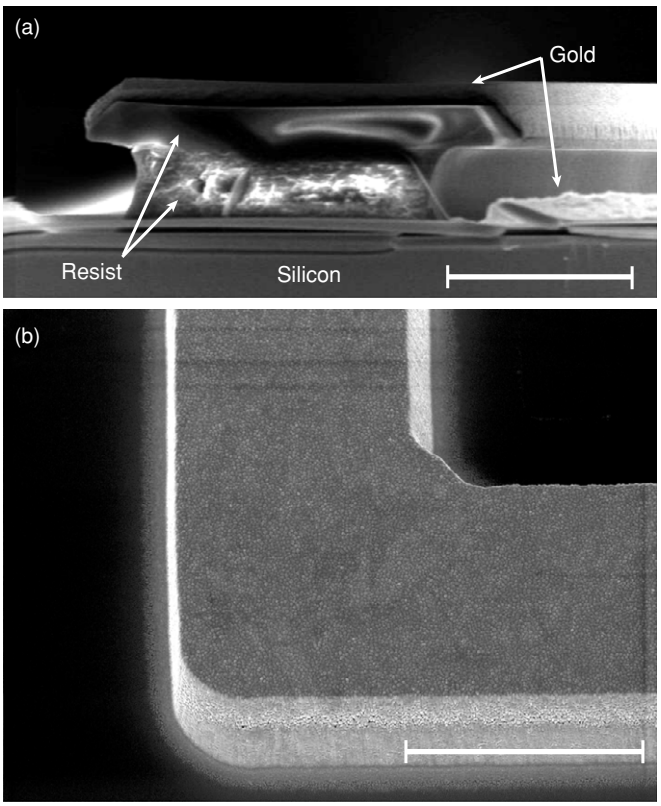

Figure 2. Scanning electron microscope (SEM) images of (a) the cross-section of the resist during fabrication of the atom chip. The undercut is clearly visible. The image was made immediately after gold evaporation and an ∼0.5 μm gold layer can be seen lying on top of the resist structure. (b) A 5 μm wide chip wire. The corner displayed is part of a wiggle used to form a box potential. The scale bars in both figures have a length of 5 μm.

(2) *Resist.* The substrate is dehydrated on a hotplate at 150 °C for 5 min prior to applying the resist. After the substrate has cooled down we spin coat (1 min at 3000 rpm) the bottom resist layer (LOR 20B) to a thickness of 2.0–2.5 μm. The substrate is then baked for 5 min at 150 °C. The top resist layer is a positive photoresist (Microposit S1813), spin coated (1 min at 5000 rpm) to a layer of 1.2 μm thickness. It is then baked for another 30 min at 90 °C.

(3) *Optical lithography.* The resist is exposed with a dose of 74 mJ cm^{-2} of 365 nm near-ultra-violet (NUV) light from a Karl Suss MJB3 mask aligner. A 4 inch Cr mask was made to specification by Deltamask (Enschede, The Netherlands) using a 442 nm HeCd laser with a resolution of ∼1 μm, based on an AutoCAD design drawing. We have found that the minimum feature size of our chips of about 3 μm is not limited by the lithography mask, but rather by scattering and divergence of the light inside the thick bilayer resist. After exposure we submerge the substrate in a Microposit MF319 developer for 1 min and then rinse in water to stop development. As the lower layer dissolves faster than the top layer an undercut is produced, extending ∼1 μm. We then expose the chip surface to a low-energy oxygen plasma for 5 min to remove remaining resist residue from the exposed silicon. This may also enhance the thin native oxide layer present (1–2 nm thick), which provides electrical isolation between the gold conductor layer and the silicon substrate but allows high thermal conductivity.

(4) *Gold deposition.* The gold layer is deposited in a PVD (physical vapour deposition) system at $\leqslant 10^{-5}$ mbar. A 10 nm thick titanium bonding layer is first deposited to provide adhesion between the silicon surface and the gold layer. Gold is then evaporated at a rate of 1 nm s^{-1} to a total thickness of 1.25 μm; the maximum possible given the crucible used can only hold 3 g of gold at a time. After a refill we continue the evaporation to 1.8 μm. The achievable thickness is ultimately limited by the thickness of the lift-off resist which must prevent filling of the insulating channels.

(5) *Lift-off.* We rest the chip in a beaker containing Microposit Remover 1165 at a temperature of 68 °C for ∼1 h to lift off the excess gold. It was helpful to create a bit of flow in the beaker with a syringe. We do not use ultrasonic agitation as that can damage the remaining gold wires. After lift-off we rinse the chip several times in acetone and iso-propanol and then use the oxygen plasma again to remove any remaining resist or solvent.

Table 1. Characteristics of the wires included on the atom chip shown in figure 1. Widths w and resistances R of the wires are listed, along with their intended functions for ongoing experiments.

Wire	w (μm)	R (Ω)	Function
1	10	3.15	Double-box structure
2	5	3.70	Wiggle test wire
3	50	1.47	*Z*-wire, radio-frequency field
4	10	3.89	1.00 mm long box
5	125	0.72	*Z*-wire, initial trapping and cooling
6	10	2.42	0.20 mm long box, rf evaporation
7	30	2.06	*Z*-wire, radio-frequency field
8	20	2.30	0.90 mm long box

3.2. Wire pattern design

The current chip design (figure 1, table 1) includes eight wires, all adjacent to the broad 125 μm wide *Z*-shaped wire which is used for initial trapping and evaporative cooling. Due to the shape of this wire, all chip wires have an unavoidable *Z* shape to prevent crossings in the single conductor layer. Wires 3 and 7 are regular *Z*-shaped wires with 3 mm long straight segments and widths of 50 and 30 μm, respectively, placed almost symmetrically on either side of the central *Z*-wire at a distance of ∼100 μm. These wires have been used with rf-currents to produce radio-frequency-dressed potentials for manipulating BECs [27]. The remaining wires have been designed to produce one-dimensional box potentials with various lengths defined by the distances between wiggle segments (table 1). Each wire is separated by 10 μm wide insulating channels in the gold layer. At the centre of the chip the exact shape and quality of the wires is crucial because of the close proximity to the trapped atoms; however, outside the central sections we allow the wires to fan out as much as possible to reduce wire resistance and ohmic heating. The long edges of the chip host 2.1 mm wide contact pads which provide ample

space to connect each wire to a contact pin on the chip mount (4.4 mm wide pads for the 125 μm Z-wire). The edges of the chip running parallel to the wires do not have contacts in order to maximize optical access for imaging.

3.3. Chip characterization

Surface and edge roughness. The quality of the magnetic potentials produced by microfabricated conducting wires depends critically on both edge and surface roughness [3, 5, 32, 33, 35]. To characterize these properties we have used a combination of optical microscopy, atomic force microscopy (AFM), scanning electron microscopy (SEM) and surface profilometry. We summarize our findings below. Figure 2 shows images of the resulting wire structures obtained with a SEM. From this and AFM measurements we find that the top surface and the sides of the wires are smooth down to the grain size of the gold (typically 50 nm). This is comparable to some of the best results reported so far in terms of potential smoothness [33, 34, 36]. The observed rounding of the wire corners seen in figure 2(b) is the result of the finite resolution of optical lithography. The two deposition layers of the gold film are also visible as a slight change in structure along the side of the wire; however, this does not appear to increase the wire surface roughness.

It is generally difficult to quantify tiny fluctuations of the wire edge over large length scales which are relevant for experiments with atoms. Using an optical microscope the wires appear perfectly straight within the optical resolution of $\sim$1 μm over length scales of hundreds of micrometres. We have also measured the flatness of the top surface of a chip wire over a distance of 800 μm using a surface profiler (KLA Tencor Alphastep 500). We find a roughness of 1.8 nm rms with correlations on the 300 μm length scale. The measured profiles are similar to those obtained on a bare Si substrate suggesting that the evaporated gold layer accurately follows the substrate surface and has an approximately uniform thickness. From these measurements we conclude that the wire patterns are fabricated with high quality and should produce very smooth potentials for atoms. Ultimately the quality of the wires is inferred from the magnetic field roughness measured using ultracold atoms as a probe (section 4.2).

Chip wire resistance. We have also measured the resistance of the chip wires under typical experimental conditions. Placed in a vacuum of 10^{-6} mbar to suppress cooling through convection, we performed a four-terminal measurement of the resistance with a current of about 100 mA (current density $\lesssim 5 \times 10^5$ A cm^{-2}), which is sufficiently low to neglect the increase in resistance due to ohmic heating. The measured resistances are $\sim$10% larger than those expected from a simple calculation, which we attribute to the additional resistance of the in-vacuum leads and wire bonds not included in the calculation.

Additional measurements of the resistance between different chip wires were performed to ensure that the insulating channels are sufficient to prevent current leakage under typical operational conditions. Immediately after fabrication the inter-wire resistances are around 200–600 kΩ, approximately 10^6 times larger than the wire resistance. These values are too large to be explained by the resistivity of the silicon alone; hence, we conclude that the resistance is mainly determined by the thin native silicon oxide surface layer, possibly enhanced by the exposure to the oxygen plasma during fabrication [37]. After 3 months of use we found that the inter-wire resistances had decreased significantly to between 1 kΩ and 60 kΩ. This is most likely attributable to diffusion of gold into the silicon-oxide layer. With the new resistances we anticipate current leakage between wires on the level of 10^{-4}, possibly causing deviations from the nominal magnetic fields at the 10 mG level. This effect appears to be accelerated by regular heating of the wires during experiments, as the lowest inter-wire resistances are measured between those wires used most frequently. After the initial decrease, the resistances appear to have stabilized at their current values. We expect this effect may be reduced in the future by incorporating a dedicated insulating top layer on the Si substrate.

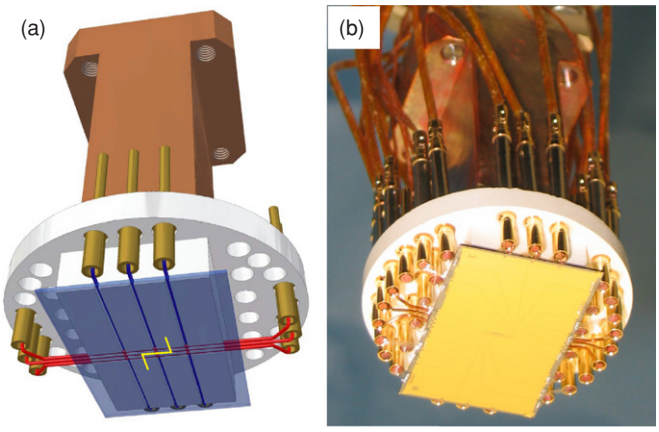

Figure 3. (a) Chip mount showing the arrangement of the two layers of miniwires. The orientation of the Z-wire is indicated at the centre of the drawing. (b) Photograph of the completed atom chip construction.

3.4. Assembly

The atom chip is mounted on a macroscopic support structure which includes six additional wires capable of carrying currents of up to 20 A for loading atoms to the chip-based microtraps (figure 3). The 300 μm diameter Kapton-coated copper 'miniwires' run in two isolated layers oriented along x and y (each with three parallel wires) positioned at $z = -0.5$ mm and $z = -0.8$ mm underneath the chip surface respectively. The separation between the wires within one layer is 0.65 mm (top layer) and 3 mm (bottom layer), for the wires along x and y respectively. These wires fit in grooves in a boron-nitride ceramic disc which has been machined by a computer-controlled milling machine. Boron nitride is easily machined and has 20 times higher thermal conductivity than Macor. The miniwires are electrically connected using standard vacuum-compatible sub-D-type gold-plated connector pins. We strip the Kapton from the end of the miniwire and press it, along with a piece of bare copper, into the male pin. The resistance of the miniwires (including the

connection to the male pins) is 10 mΩ. Operated at a current of 10 A, the power dissipation is 1 W per wire over its whole length, resulting in negligible heating (10 K W^{-1}).

The Boron nitride disc is bonded using Epo-tek H77 epoxy to a copper heat sink mount made of oxygen-free high-conductance (OFHC) copper. This is bolted to the end cap of a hollow stainless-steel (type 316 L) rod with an outer (inner) diameter of 16 mm (8 mm) which is welded to a CF40 flange for insertion into the vacuum system. The chip can be water cooled by means of a polyvinyl chloride (PVC) tube of 6 mm diameter which runs coaxially inside the stainless-steel rod. We typically run 0.1 l min^{-1} of cold tap water through the system during operation. At night this supply is replaced by heated water at 40 °C intended to limit the amount of Rb collected on the chip surface.

In the final assembly the microchip is carefully glued to the ceramic disc using Epo-tek 377 epoxy. The alignment error between the on-chip *Z*-wire and the miniwires was found to be smaller than 50 μm. The eight chip wires are connected to the contact pins with 20 μm diameter aluminium wires with a wire bonding technique. Each contact pad was bonded with ten wires except for the *Z*-wire where we have used 14 wire bonds to sustain higher currents. The chip wires are then connected to a set of sub-D-type vacuum feedthroughs. The maximum bakeout temperature for the chip mount in the vacuum system is 180 °C, limited by the Kapton-coated wires and the epoxy. The entire chip setup is compatible with ultrahigh vacuum, and after bakeout operates at a pressure of 10^{-10} mbar.

4. Ultracold atoms

To demonstrate the suitability of the produced potentials for studying ultracold atoms and quantum gases we have loaded the $L = 1$ mm box-shaped trap (wire 4 in figure 1). This allows the resulting magnetic potentials to be characterized using the atoms as a probe. We demonstrate evaporative cooling of atoms confined in the box trap and apply the method of Bose-gas focusing [9, 28, 29] to perform thermometry of atom clouds.

4.1. Loading ultracold atoms in the box trap

A cloud of ^{87}Rb atoms is initially collected from the background vapour by a mirrorMOT positioned below the chip surface. We then apply a polarization gradient cooling stage and optical pumping to the atoms in preparation for magnetic trapping. The spin-polarized atoms are first trapped in an Ioffe–Pritchard magnetic trap formed by the miniwires underneath our chip (figure 3). For best mode-matching we make this trap as weak as possible while maintaining sufficient confinement to hold the atoms against gravity. We then immediately transfer the atoms to a trap formed by the *Z*-wire on the chip by ramping down the miniwire currents within 30 ms. Approximately 2×10^7 atoms in the $F = 2, m_F = 2$ state are caught in a magnetic trap at $z \approx 400$ μm produced by the central *Z*-shaped wire ($I_z = 2.25$ A) and an external field ($B_{0y} = 13$ G). This field is then ramped up to $B_{0y} = 48$ G over 200 ms to compress the trap and move to ~100 μm from the surface. The central miniwire remains on at 2.7 A which produces a dimple in the longitudinal potential to improve evaporative cooling efficiency. Next, a logarithmic radio frequency sweep from 27 MHz to 2.1 MHz is applied over 750 ms to evaporatively cool the atoms to a few microkelvin. The radio frequency is then increased again to 2.3 MHz prior to transferring the cloud to the box potential.

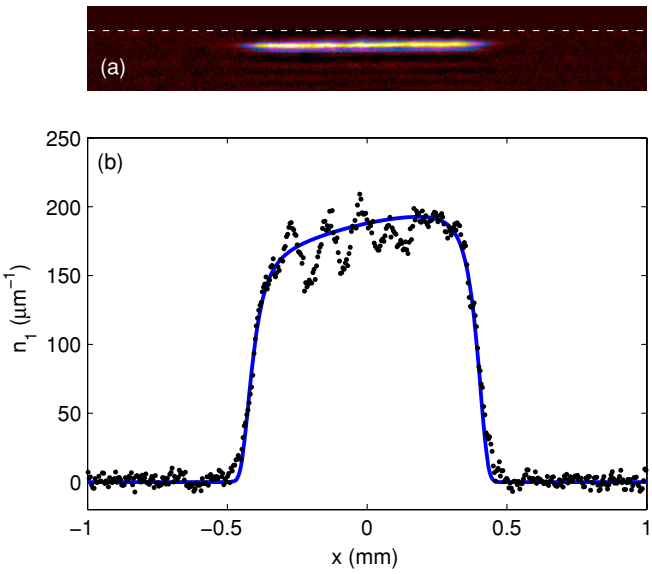

Figure 4. *In situ* atomic density distribution after loading the box-shaped potential for a final evaporation radio frequency of 1.80 MHz. (a) Optical density image showing a 70 × 465 pixel region (4.3 μm pixel size in the object plane). The dashed line indicates the approximate position of the chip surface. (b) Integrated profile showing the corresponding linear atomic density n_1 as a function of the longitudinal position x. The solid line is a result from the analysis in section 4.3 for the expected in-trap density distribution corresponding to a temperature of $T = 4.16$ μK.

To transfer, we first weaken the confinement of the *Z*-wire trap and increase the trap-surface distance to ~200 μm by reducing the bias field to $B_{0y} = 20$ G within 50 ms. In 25 ms the *Z*-wire current is ramped down to 1 A while the current in the adjacent box wire is increased to 0.8 A to position the cloud between the two wires. Finally, the *Z*-wire current is ramped off completely and the box wire current is reduced to 0.37 A with another 25 ms ramp.

A final cooling stage is applied to the atoms in the box trap using a two-part rf sweep, first from 2.30 MHz to 1.95 MHz in 60 ms and next from 1.95 MHz to a final frequency between 1.80 MHz and 1.41 MHz in 50 ms. The trap bottom as measured using rf spectroscopy is at 1.40 MHz. After evaporation the rf amplitude is switched off completely. Atoms are imaged by turning off the trap, waiting for a variable time-of-flight and then applying a resonant probe laser pulse to the atoms. The shadow created by the atomic distribution is then imaged to a CCD camera for analysis. The effective pixel size in the object plane is 4.3 μm and the optical resolution is 4 μm.

4.2. Box potential

Figure 4 shows an optical density image of the atom cloud after transfer to the box potential for a final radio frequency

of 1.80 MHz. We observe an elongated square-top profile for the atomic distribution as expected for a Boltzmann gas at thermal equilibrium in the box-shaped potential defined by equation (2). We note that the distributions are slightly asymmetric for final radio frequencies above 1.50 MHz (corresponding to higher cloud temperatures), but become increasingly asymmetric as the radio frequency is reduced (to lower cloud temperatures). We attribute this to a small potential gradient, possibly a tilt of the chip surface with respect to gravity.

Additionally, we observe time-independent optical density modulations in the axial profiles. We have estimated the magnetic field inhomogeneity that could cause such modulations from the data presented in figure 4 and with additional data for various temperatures between 0.28 and 4.16 μK. This was performed using a procedure similar to previous experiments in the 1D regime [38, 39], but for thermal atom distributions [32, 35, 40]. The observed density modulations do not scale with cloud temperature as would be expected for potential corrugations; their amplitude is roughly 20% of the peak density and independent of temperature. Secondly, the modulations are correlated on length scales comparable to intensity variations present in the raw absorption (and reference) images ($\approx$100 μm). Based on these observations we attribute the modulations to imaging artefacts due to the nearby chip surface rather than potential corrugations. The observed modulations do however provide an upper limit for the possible potential variations experienced by atoms in the box trap. From the amplitude of the density modulations for the hottest temperature (4.16 μK) we infer an upper bound on the potential roughness of $\Delta V/k_B \leqslant 130$ nK (with k_B Boltzmann's constant) or $\Delta B \leqslant 1.9$ mG rms for a wire current of 0.37 A and a height of $z = 40$–50 μm. The figure of merit for the box trap is thus $\Delta B/B_{0y} \approx 1 \times 10^{-4}$ which compares well to other chip traps [32, 33]. The measured value is consistent with previous measurements on the broader Z-shaped wire for which we determine $\Delta B/B_{0y} < 5 \times 10^{-5}$ for a height of $z = 120$ μm [27, 30].

The following calculation shows that this trap can support quantum gases in the 1D regime. To support an unfragmented 1D quasi-condensate (with $\mu < \hbar\omega_\perp$) requires that $m_F g_F \mu_B \Delta B < \hbar\omega_\perp$. We estimate the transverse confinement for the parameters used in experiments as $\omega_\perp/2\pi \approx 4$ kHz. This corresponds to a thermal excitation energy of $\approx$200 nK, which is greater than the upper bound for the potential corrugations of 130 nK and satisfies the above constraints. A 1D zero-temperature condensate in this trap would fragment for linear densities below $n_1 = 100$ μm^{-1}. Lower linear densities can be reached without significant modifications using time-dependent potentials to smoothen the corrugated potential [27, 33, 41]. Alternatively, strong transverse confinement while minimizing corrugation could be provided by an auxiliary wire located far from the atoms [38], with the walls of the box trap produced by a small current in the box-shaped wire. Due to the steep walls provided by the wiggle wires, currents less than $\sim$10 mA would be sufficient to provide good longitudinal confinement.

4.3. Bose-gas focusing

Bose-gas focusing is a powerful experimental approach for measuring the axial momentum distribution of harmonically trapped ultracold gases. In particular it has been applied to study non-equilibrium dynamics of BECs [28] and to equilibrium systems in the crossover from the three-dimensional to the one-dimensional regimes [9, 31]. Here, we extend the description to arbitrarily shaped axial potentials, and apply this to extract temperatures of atom clouds in box-shaped potentials. This technique is particularly relevant for one-dimensional gases in box-shaped traps as the spatial distribution of atoms depends weakly on temperature and conventional thermometry methods fail.

The concept of atom focusing of an elongated cloud is as follows: initially, the atoms are in thermal equilibrium in the confining potential. A relatively strong parabolic (harmonic) potential is switched on in the axial direction. This is applied for a short time, typically smaller than the oscillation period, before being switched off. This pulse gives a kick to the atoms which is proportional to their distance from the trap centre and is analogous to the action of a lens in optics [29]. Then the atoms are released from the trap and allowed to evolve during a period of free propagation. The effect of the kick brings the atoms to an axial focus at a time t_{focus}. At this point the distribution has a minimum axial width proportional to the cloud temperature and the in-focus distribution reflects the axial momentum distribution prior to focusing.

In a classical description, suitable for a non-degenerate gas, the time evolution of the atomic distribution induced by the focusing action can be expressed by

$$\begin{aligned} g(t) &= a(t)x_0 + b(t)v_0 \\ h(t) &= c(t)x_0 + d(t)v_0, \end{aligned} \tag{3}$$

where the final position $g(t)$ and velocity $h(t)$ of an atom depend on the initial position and velocity x_0, v_0 through the focus parameters a, b, c and d. These parameters directly correspond to those in the $ABCD$ matrix formalism known from conventional (ray- and gaussian-beam) optics [42]. Transformation of the phase space distribution $f(x, v, t)$ by this evolution is given by

$$f(x, v, t) = \iint f(x_0, v_0, 0)\delta(x - g(t))\delta(v - h(t))\,\mathrm{d}x_0\,\mathrm{d}v_0 \tag{4}$$

with $\delta(\,)$ the Dirac delta function. From this it is possible to determine the real space atomic density distribution $n(x, t) = \int f(x, v, t)\mathrm{d}v$. This is conveniently expressed in terms of the initial distribution

$$n(x, t) = \frac{1}{|b(t)|}\int f\left(x_0, \frac{x - a(t)x_0}{b(t)}, 0\right)\mathrm{d}x_0. \tag{5}$$

Thus, we are left with a single integral over the modified initial phase-space distribution.

We assume a classical gas in thermal equilibrium given by the Boltzmann law:

$$f(x_0, v_0, 0) = C\exp\left[-\frac{1}{k_B T}\left(\frac{1}{2}mv_0^2 + V(x_0)\right)\right] \tag{6}$$

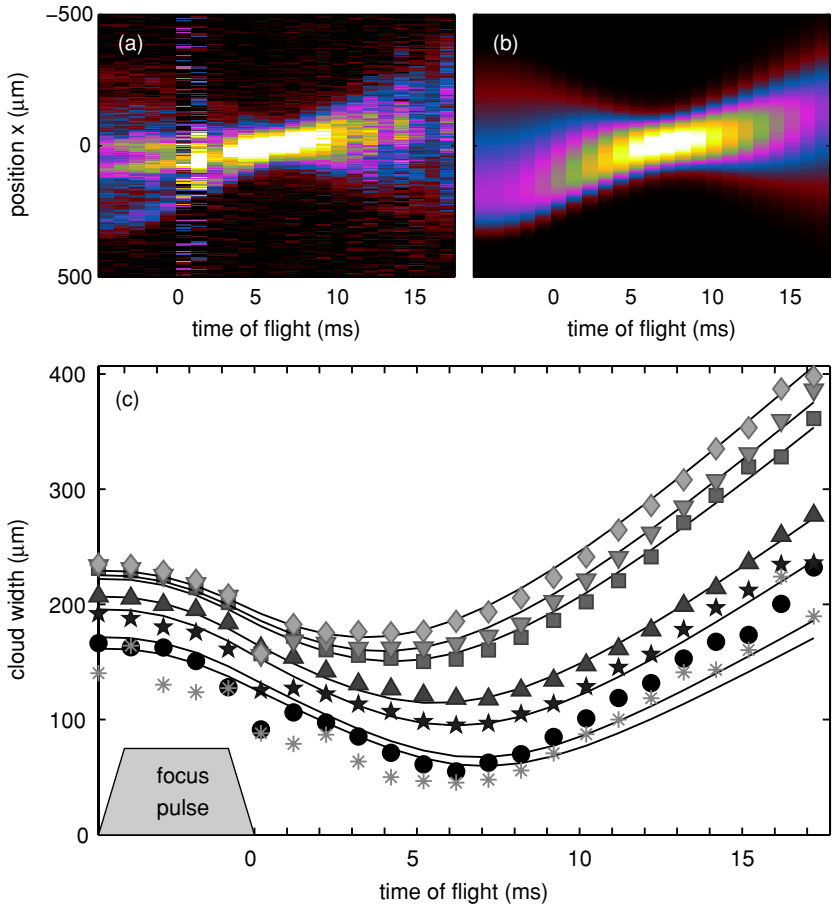

Figure 5. Focusing ultracold atoms from a box-shaped potential. (a) Measured optical density profiles during the focus sequence. (b) Calculated profiles based on the focusing model of equation (7). (c) Cloud width during the focus sequence for several values of the final evaporation radio frequency and corresponding fits used to determine the cloud temperature. Symbols (curves) correspond to final radio frequencies (fitted temperatures) of ⋄ 1.80 MHz (4.16 μK), ∇ 1.70 MHz (3.44 μK), □ 1.64 MHz (2.95 μK), △ 1.50 MHz (1.51 μK), ⋆ 1.46 MHz (1.02 μK), • 1.42 MHz (0.42 μK) and ∗ 1.41 MHz (0.28 μK). The shape and duration of the focus pulse is indicated by the shaded area.

where $V(x_0)$ is the confining potential energy and C is a normalization constant which yields the total number of atoms. Inserting this initial distribution in equation (5) gives

$$n(x,t) = \frac{1}{|b(t)|v_T\sqrt{\pi}} \times \int n(x_0)\exp\left[-\left(\frac{x-a(t)x_0}{b(t)v_T}\right)^2\right]\mathrm{d}x_0 \tag{7}$$

with the thermal velocity $v_T = \sqrt{2k_BT/m}$. The density distribution during time-of-flight depends on the initial density distribution $n(x_0) = n_0\exp[-(V(x_0) - V_0)/kT]$ where n_0 is the peak atomic density and V_0 is the potential energy at the trap minimum.

For a harmonic focusing pulse with a duration t_p and strength ω followed by a period of free evolution t, the relevant evolution parameters are given by

$$\begin{aligned} a(t) &= \cos(\omega t_p) - \omega t\sin(\omega t_p) \\ b(t) &= \omega^{-1}\sin(\omega t_p) + t\cos(\omega t_p). \end{aligned} \tag{8}$$

Equations (7) and (8) describe the one-dimensional spatial distribution of ultracold atoms during and after the application of a parabolic focusing pulse for an arbitrary shaped initial potential $V(x_0)$. In the following, we apply this model to analyse our experimental results for focusing from the box-shaped potential of equation (2).

Results of the focusing experiments are shown in figure 5. To perform the measurements we first increase the axial offset magnetic field by 4.25 G within 50 ms. To push the atoms away from the chip surface the box wire current is increased to 0.95 A in 2 ms. This is followed by a short trapezoidal current pulse applied to the miniwires beneath and perpendicular to the box wire to temporarily introduce a parabolic axial potential. This pulse consists of a 0.8 ms linear ramp to 0.45 A and 9.8 A for the central and outer miniwires respectively, held constant for 4 ms, then finally turned off again in 0.8 ms. The pulse amplitude corresponds to a peak axial oscillation frequency of $\omega = 2\pi \times 25$ Hz. Finally all the fields are switched off ($t = 0$) and the atomic distribution is allowed to freely evolve while falling under gravity. During the pulse ($t < 0$) or after a variable time-of-flight ($t > 0$) between $t = -4.8$ ms and $t = 17.2$ ms an optical density image of the distribution is recorded. The image is then integrated over the radial coordinate to produce a profile of the linear atomic density.

Profiles for each time-of-flight are then compiled into a two-dimensional data set $n_1(x, t)$. An example of one such data set is shown in figure 5(a). In total we obtain seven data sets, each for a different value of the final radio frequency corresponding to a range of trap depths and final cloud temperatures.

To analyse the data we numerically perform least-squares minimization using the Nelder–Mead method to the model of equation (7) in order to determine the temperature T for each value of the final trap depth. The shape of the initial confining potential is calculated from the known wire geometry. We use the approximation of equation (2) with the box length $L = 1040$ μm, wiggle size $b = 20$ μm and trap height $z = 50$ μm. The residual harmonic confinement due to the ends of the box wire corresponds to a curvature of 1.5 μK mm^{-2} or $\omega_\parallel = 2\pi \times 2.7$ Hz. One additional parameter specifying an additional gradient to the potential is required to fully reproduce the observed density distributions and was determined to be $\Delta = -1.0$ μK mm^{-1}. This gradient would be consistent with a tilt of the chip surface with respect to gravity of less than 11 mrad, highlighting the sensitivity of such systems to small forces [43].

The focus model provides the expected spatial distribution of atoms before the focus pulse and agrees well with the measured distribution for each value of the final radio frequency, see for example figures 5(a) and (b). The focus pulse is modelled with two parameters, the pulse amplitude ($\omega/2\pi = 25$ Hz in equation (8)) and a small displacement between the centre of the parabolic potential and the box potential which causes a small kick to the cloud visible in figures 5(a) and (b) as an upward slope in the cloud centre of mass. Finally fitting is performed with temperature T for each data set as the only free parameter. The measurements and the result of this fitting procedure are shown in figures 5(a) and (b) for the 1.50 MHz data set. Good agreement is found for the full range of time-of-flights and the model accurately reproduces the focus region around $t = 6$ ms. The results for all trap depths are shown in figure 5(c), where the cloud width defined as the second central moment of the distribution is plotted. In this definition a perfect square-top distribution with length $L = 1$ mm equates to a width of $L/2\sqrt{3} = 0.29$ mm. The widths of the observed density profiles are shown with symbols, while the widths of the model distribution are shown with connected lines. For all data between 1.80 MHz and 1.46 MHz we obtain excellent agreement between the measured widths and the model distribution. Some deviation is visible for the lower temperature data sets which may be attributed to deviations from Boltzmann statistics resulting in a tighter focus than predicted by the model. For the measurements we determine the temperatures indicated in the caption of figure 5. The fitted temperatures are also consistent with measurements obtained by fitting the radial expansion rate in order to directly determine the thermal velocity.

5. Discussion and conclusion

We have implemented and experimentally investigated simple box-shaped potentials for trapping ultracold quantum gases on an atom chip. Our chip hosts a series of long, thin and straight current-carrying wires which create extremely elongated traps, presently used in studies of Bose gases in one dimension and in radio-frequency-dressed potentials [9, 27]. The described fabrication procedure is tailored for relatively thick wires for high current capacities and with high surface and edge quality to produce smooth trapping potentials. We investigate the quality and suitability of the resulting potentials by loading ultracold atoms into a 1 mm long box-shaped trap at a distance of $z \approx 50$ μm. The observed linear density profile has a square-top shape, as expected for a thermal gas in the box-shaped potential, with small density modulations from which we infer a potential roughness of $\leqslant$130 nK rms. Finally, we have extended the technique of Bose-gas focusing to arbitrarily shaped axial potentials and applied the method to measure the energy distribution of thermal clouds prepared in the box-shaped trap between 0.28 μK and 4.16 μK. We expect this thermometry technique to be particularly valuable for one-dimensional systems, as the radial expansion velocity becomes independent of temperature. Furthermore, in an ideal box trap the spatial distribution of atoms is independent of the cloud temperature thereby limiting the application of conventional thermometry techniques. Our results show that box-shaped potentials implemented on an atom chip are very promising for the study of one-dimensional quantum gases.

Acknowledgments

We gratefully acknowledge R J C Spreeuw, T Gregorkiewicz, G V Shlyapnikov and J T M Walraven for helpful discussions. The atom chip was produced and characterized using the facilities of the Amsterdam nanoCenter and with the help of J Rövekamp. This work is part of the research program of the Stichting voor Fundamenteel Onderzoek van de Materie (Foundation for the Fundamental Research on Matter), and was made possible by financial support from the Nederlandse Organisatie voor Wetenschappelijk Onderzoek (Netherlands Organization for the Advancement of Research) and by the European Union through contract MRTN-CT-2003-505032 ('Atom Chips'), and a Marie Curie fellowship (SW, grant number PIIF-GA-2008-220794).

References

[1] Folman R, Krüger P, Schmiedmayer J, Denschlag J and Henkel C 2002 *Adv. At. Mol. Opt. Phys.* **48** 263
[2] Reichel J 2002 *Appl. Phys.* B **74** 469
[3] Fortágh J and Zimmermann C 2007 *Rev. Mod. Phys.* **79** 235
[4] Reichel J and Thywissen J H 2004 *J. Phys. IV (France)* **116** 265
[5] Della Pietra L, Aigner S, vom Hagen C, Groth S, Bar-Joseph I, Lezec H J and Schmiedmayer J 2007 *Phys. Rev.* A **75** 063604
[6] Trebbia J-B, Estève J, Westbrook C I and Bouchoule I 2006 *Phys. Rev. Lett.* **97** 250403
[7] Jo G-B, Choi J-H, Christensen C, Lee Y-R, Pasquini T, Ketterle W and Pritchard D 2007 *Phys. Rev. Lett.* **99** 240406
[8] Hofferberth S, Lesanovsky I, Fischer B, Schumm T and Schmiedmayer J 2007 *Nature* **449** 324
[9] van Amerongen A H, van Es J J P, Wicke P, Kheruntsyan K V and van Druten N J 2008 *Phys. Rev. Lett.* **100** 090402

[10] Bouchoule I, van Druten N J and Westbrook C 2010 Atom chips and one-dimensional Bose gases *Atom Chips* ed J Reichel and V Vuletic (New York: Wiley) in press (arXiv:0901.3303)
[11] Petrov D S, Gangardt D M and Shlyapnikov G V 2004 *J. Phys. IV* **116** 5
[12] Bloch I, Dalibard J and Zwerger W 2008 *Rev. Mod. Phys.* **80** 885
[13] Lieb E H and Liniger W 1963 *Phys. Rev.* **130** 1605
[14] Yang C N and Yang C P 1969 *J. Math. Phys.* **10** 1115
[15] Korepin V E, Bogoliubov N M and Izergin A G 1993 *Quantum Inverse Scattering Method and Correlation Functions* (Cambridge: Cambridge University Press)
[16] Takahashi M 1999 *Thermodynamics of One-Dimensional Solvable Models* (Cambridge, UK: Cambridge University Press)
[17] Kheruntsyan K V, Gangardt D M, Drummond P D and Shlyapniknov G V 2003 *Phys. Rev. Lett.* **91** 040403
[18] Yurovsky V A, Olshanii M and Weiss D S 2008 *Adv. At. Mol. Opt. Phys.* **55** 61
[19] Olshanii M 1998 *Phys. Rev. Lett.* **81** 938
[20] Gaudin M 1971 *Phys. Rev.* A **4** 386
[21] Batchelor M T, Guan X W, Oelkers N and Lee C 2005 *J. Phys. A: Math. Gen.* **38** 7787
[22] de Groot S R, Hooyman G J and ten Seldam C A 1950 *Proc. R. Soc.* A **203** 266
[23] Ketterle W and van Druten N J 1996 *Phys. Rev.* A **54** 656
[24] van Druten N J and Ketterle W 1997 *Phys. Rev. Lett.* **79** 549
[25] Kheruntsyan K V, Gangardt D M, Drummond P D and Shlyapnikov G V 2005 *Phys. Rev.* A **71** 053615
[26] Meyrath T P, Schreck F, Hanssen J L, Chuu C-S and Raizen M G 2005 *Phys. Rev.* A **71** 041604
[27] van Es J J P, Whitlock S, Fernholz T, van Amerongen A H and van Druten N J 2008 *Phys. Rev.* A **77** 063623
[28] Shvarchuck I, Buggle C, Petrov D S, Dieckmann K, Zielonkowski M, Kemmann M, Tiecke T G, von Klitzing W, Shlyapnikov G V and Walraven J T M 2002 *Phys. Rev. Lett.* **89** 270404
[29] Riou J-F, Coq Y L, Impens F, Guerin W, Bordé C J, Aspect A and Bouyer P 2008 *Phys. Rev.* A **77** 033630
[30] van Es J J P 2009 *PhD Thesis* Universiteit van Amsterdam
[31] van Amerongen A H 2008 *PhD Thesis* Universiteit van Amsterdam
van Amerongen A H 2008 *Ann. Phys. Fr.* **33** (3) 1–94
[32] Estève J, Aussibal C, Schumm T, Figl C, Mailly D, Bouchoule I, Westbrook C I and Aspect A 2004 *Phys. Rev.* A **70** 043629
[33] Krüger P, Andersson L M, Wildermuth S, Hofferberth S, Haller E, Aigner S, Groth S, Bar-Joseph I and Schmiedmayer J 2007 *Phys. Rev.* A **76** 063621
[34] Groth S, Krüger P, Wildermuth S, Folman R, Fernholz T, Schmiedmayer J, Mahalu D and Bar-Joseph I 2007 *Appl. Phys. Lett.* **85** 2980
[35] Schumm T, Estève J, Figl C, Trebbia J-B, Aussibal C, Nguyen H, Mailly D, Bouchoule I, Westbrook C I and Aspect A 2005 *Eur. Phys. J.* D **32** 171
[36] Trinker M, Groth S, Haslinger S, Manz S, Betz T, Scheider S, Bar-Joseph I, Schumm T and Schmiedmayer J 2008 *Appl. Phys. Lett.* **92** 254102
[37] Nicollian E and Brews J R 1982 *MOS (Metal Oxide Semiconductor) Physics and Technology* (New York: Wiley)
[38] Wildermuth S, Hofferberth S, Lesanovsky I, Haller E, Andersson M, Groth S, Bar-Joseph I, Krüger P and Schmiedmayer J 2005 *Nature* **435** 440
[39] Wildermuth S, Hofferberth S, Lesanovsky I, Groth S, Krüger P and Schmiedmayer J 2006 *Appl. Phys. Lett.* **88** 264103
[40] Aigner S, Pietra L D, Japha Y, Entin-Wohlman O, David T, Salem R, Folman R and Schmiedmayer J 2008 *Science* **319** 1226
[41] Trebbia J-B, Garrido Alzar C L, Cornelussen R, Westbrook C I and Bouchoule I 2007 *Phys. Rev. Lett.* **98** 263201
[42] Siegman A E 1986 *Lasers* (Mill Valley, CA: University Science Books)
[43] Hall B V, Whitlock S, Anderson R, Hannaford P and Sidorov A I 2007 *Phys. Rev. Lett.* **98** 030402